IAEA nuclear fusion

Simulations of energetic particle driven instabilities in CFQS

Simulations of energetic particle driven instabilities in CFQS

Hao WANG (王 灏)[1], Yasushi TODO (藤堂 泰)[1], Jie HUANG (黄 杰)[2,3], Yasuhiro SUZUKI (鈴木 康浩)[4], Akihiro SHIMIZU (清水 昭博)[1], Kunihiro OGAWA (小川 国大)[1], Xianqu WANG (王 先驱)[5], Panith ADULSIRISWAD[1]

[1]National Institute for Fusion Science, National Institutes of Natural Sciences, Toki, Japan

[2]Forschungszentrum Jülich GmbH, Jülich, Germany

[3]Huazhong University of Science and Technology, Wuhan, China

[4]Hiroshima University, Higashihiroshima, Japan

[5]Southwest Jiaotong University, Chengdu, China

E-mail: `wanghao@nifs.ac.jp`

July 25, 2022

Abstract. A nonlinear simulation of the energetic particle driven instabilities in the Chinese First Quasi-Axisymmetric Stellarator (CFQS) has been conducted for the first time. MEGA, a hybrid simulation code for energetic particles interacting with a magneto-hydrodynamic (MHD) fluid, was used in the present work. Both the $m/n = 3/1$ energetic-particle-mode (EPM) like mode and the $m/n = 5/2$ toroidal Alfvén eigenmode (TAE) were found, where m is the poloidal mode number and n is the toroidal mode number. Four important results were obtained as follows. First, the instability in the CFQS in three-dimensional form was shown for the first time. Second, strong toroidal mode coupling was found for the spatial profiles, and it is consistent with the theoretical prediction. Third, the resonant condition caused by the absence of axial symmetry in CFQS was demonstrated for the first time. The general resonant condition is $f_{mode} = Nf_\phi - Lf_\theta$, where f_{mode}, f_ϕ, and f_θ are mode frequency, particle toroidal transit frequency, and particle poloidal transit frequency, respectively; N and L are arbitrary integers, represent toroidal and poloidal resonance numbers. For EPM-like mode, the dominant and subdominant resonant conditions are $f_{mode} = 3f_\phi - 7f_\theta$ and $f_{mode} = f_\phi - f_\theta$, respectively. For TAE, the dominant and subdominant resonant conditions are $f_{mode} = 4f_\phi - 9f_\theta$ and $f_{mode} = 2f_\phi - 3f_\theta$, respectively. On the one hand, the toroidal resonance numbers are different from the toroidal mode numbers by 2. This indicates that the 2-fold rotational symmetry affects the resonance condition. On the other hand, the subdominant resonances satisfy $N = n$, which is expected for the axisymmetric plasmas and most of the toroidal plasmas including stellarators. Fourth, the nonlinear frequency chirpings in CFQS were demonstrated for the first time. Hole and clump structures were formed in the pitch angle and energy phase space, and the particles comprising the hole and clump were kept resonant with the modes during the mode frequencies chirping.

1. Introduction

Nuclear fusion may solve the energy crisis of human beings. For magnetic confinement fusion, the most important two kinds of devices are the tokamak and stellarator. The tokamak is good for reducing neoclassical transport, and the stellarator for steady state operation. The QA device is a kind of tokamak-like stellarator, or a combination of tokamak and stellarator. On the one hand, as a stellarator it does not require inductive plasma current, and thus it is very appropriate for steady state operation; on the other hand, because of its special quasi-symmetric configuration, it weakens the neoclassical transport, and thus the confinement level is better than a conventional stellarator[1]. Because of these advantages, two QA devices, the CHS-qa[2] and NCSX[3], were designed many years ago in Japan and the USA, respectively. Also, the QuASDEX is being designed in Germany. Now a QA device named the Chinese First Quasi-Axisymmetric Stellarator (CFQS) is being constructed by National Institute for Fusion Science (Japan) and Southwest Jiaotong University (China) under a framework of international collaboration. The first plasma will be generated soon[4, 5]. After that auxiliary heating, including both electron cyclotron resonance heating (ECRH) and NBI, will be applied. Many studies based on the CFQS have already been carried out and they cover different topics like configuration optimization, MHD instabilities, energetic particle driven instabilities, etc.[6–8]

Energetic particle driven instability is an important issue for fusion research. During energetic particle driven instabilities, the radial transport of energetic particles will be enhanced and a lot of energetic particles lost, and thus heating performance will deteriorate, and the confinement level will decrease. The Alfvén eigenmode (AE) is a typical dangerous energetic particle driven instability. During AE activities more than half of energetic particles can be lost[9]. Thus it is important to investigate the AE properties in the CFQS before its first plasma, in order to avoid a dangerous configuration or operation. Similarly, the energetic-particle-mode (EPM) is also dangerous for its large amplutude and strong transport effect[10–12].

The AE behaviors in the CFQS have already been investigated in Ref. [8]. The linear properties of many different AEs including $m/n = 3/1$ mode and $m/n = 5/2$ mode were analyzed under various conditions like the rotational transform ι profiles and plasma pressure profiles. As the first literature of AE properties in the CFQS, Ref. [8] covers many issues of interest, but there are still a lot of gaps left, for example nonlinear mode properties, resonant conditions, 3-dimensional visualization, and energetic particle transport. The present paper will fill in the above gaps and it is organized as follows. In section 2 the simulation model and conditions are described. In section 3 the simulation results of an EPM-like mode are presented. In section 4 the simulation results of the toroidal Alfvén eigenmode (TAE) are presented. In section 5 the main conclusions are summarized.

2. Simulation model and parameters

A hybrid simulation code, MEGA[13–15], for energetic particles interacting with a magnetohydrodynamic (MHD) fluid is used for the simulations of the energetic particle driven instabilities in the CFQS. The hybrid model is widely used in the fusion community[16]. There are two versions of MEGA. In the conventional version, only the energetic particles are described by the kinetic equations, while in the extended version both the energetic particles and the thermal ions are described kinetically. In the present work, the conventional version is applied. The MHD equations with the energetic-ion effects are given by

$$\frac{\partial \rho}{\partial t} = -\nabla \cdot (\rho \mathbf{v}) + \nu_n \triangle (\rho - \rho_{eq}), \tag{1}$$

$$\begin{aligned} \rho \frac{\partial}{\partial t}\mathbf{v} = & - \rho \boldsymbol{\omega} \times \mathbf{v} - \rho \nabla (\frac{v^2}{2}) - \nabla p + (\mathbf{j} - \mathbf{j}'_h) \\ & \times \mathbf{B} - \nabla \times (\nu \rho \boldsymbol{\omega}) + \frac{4}{3}\nabla(\nu\rho\nabla\cdot\mathbf{v}), \end{aligned} \tag{2}$$

$$\frac{\partial \mathbf{B}}{\partial t} = -\nabla \times \mathbf{E}, \tag{3}$$

$$\begin{aligned} \frac{\partial p}{\partial t} = & - \nabla \cdot (p\mathbf{v}) - (\gamma - 1) p \nabla \cdot \mathbf{v} \\ & + (\gamma - 1)[\nu \rho \omega^2 + \frac{4}{3}\nu\rho(\nabla\cdot\mathbf{v})^2 + \eta \mathbf{j}\cdot(\mathbf{j} - \mathbf{j}_{eq})] \\ & + \nu_n \triangle (p - p_{eq}), \end{aligned} \tag{4}$$

$$\mathbf{E} = -\mathbf{v} \times \mathbf{B} + \eta(\mathbf{j} - \mathbf{j}_{eq}), \tag{5}$$

$$\boldsymbol{\omega} = \boldsymbol{\nabla} \times \mathbf{v}, \tag{6}$$

$$\mathbf{j} = \frac{1}{\mu_0}\nabla \times \mathbf{B}, \tag{7}$$

where μ_0 is the vacuum magnetic permeability, γ is the adiabatic constant, ν and ν_n are artificial viscosity and diffusion coefficients, chosen to maintain numerical stability, and all the other quantities are conventional. The subscript h denotes hot particles, and in the present work, the hot particles represent energetic ones. We avoid using the subscript EP to keep consistent with previous literature. The subscript 'eq' represents equilibrium variables. The MHD equations are solved using a fourth order (in both space and time) finite difference scheme.

The energetic particles are described by the drift-kinetic equations. The modules of gyrokinetic approach is included in MEGA, but the gyrokinetic module is turned off in the simulations presented in this paper, because of three reasons: (1) the Larmor radius of energetic particle ρ_{EP} in CFQS is very small and the product of the perpendicular wave number and ρ_{EP} is much less than the unity; (2) normally the mode linear properties like frequency and mode structure are only weakly influenced by finite Larmor radius effect[17, 18]; and (3) drift-kinetic approach is more efficient for computing resources. The δf particle-in-cell (PIC) method is applied, and the equations of motion for each marker particle are solved using a fourth order Runge-Kutta method. For more details of the equations of MEGA, Ref. [13–15, 19] may be good references.

Both the VMEC and HINT codes are popular ones for plasma equilibrium[20, 21]. Although the HINT equilibrium data needs to be calculated based on the existing VMEC equilibrium data, and HINT takes much more computational resources than VMEC, HINT still has two obvious advantages for MEGA simulation. First, HINT can model complex magnetic field structures such as magnetic islands, which means that the results of HINT are closer to the real situation. Second, HINT uses (R,ϕ,z) coordinates, which are the same as MEGA, thus the equilibrium data generated by HINT can be used in MEGA more conveniently without coordinate conversion. Because of the above two advantages, in the present paper, HINT equilibria data are used for the simulation. The existing VMEC equilibrium data describes a representative case in the CFQS. Based on the existing VMEC equilibrium data, by adjusting the plasma current to 5 kA and 20 kA, finally, two different HINT equilibria data are generated. The MEGA simulation in the present paper is implemented based on these two equilibria data. They correspond to the case with magnetic islands and that without a magnetic island, as shown in Fig.1. The HINT equilibrium is not the same as the VMEC equilibrium, which can be seen from Fig. 2. For the case with magnetic islands, the pressure profile is significantly flattened near the plasma edge, which corresponds to those six magnetic islands in Fig. 1(a). In addition, the ι profile is also slightly different in these cases, as shown in Fig. 3. For the case with magnetic islands, the ι profile intersects $\iota = 1/3$ line near the plasma edge, which corresponds to those six magnetic islands in Fig. 1(a).

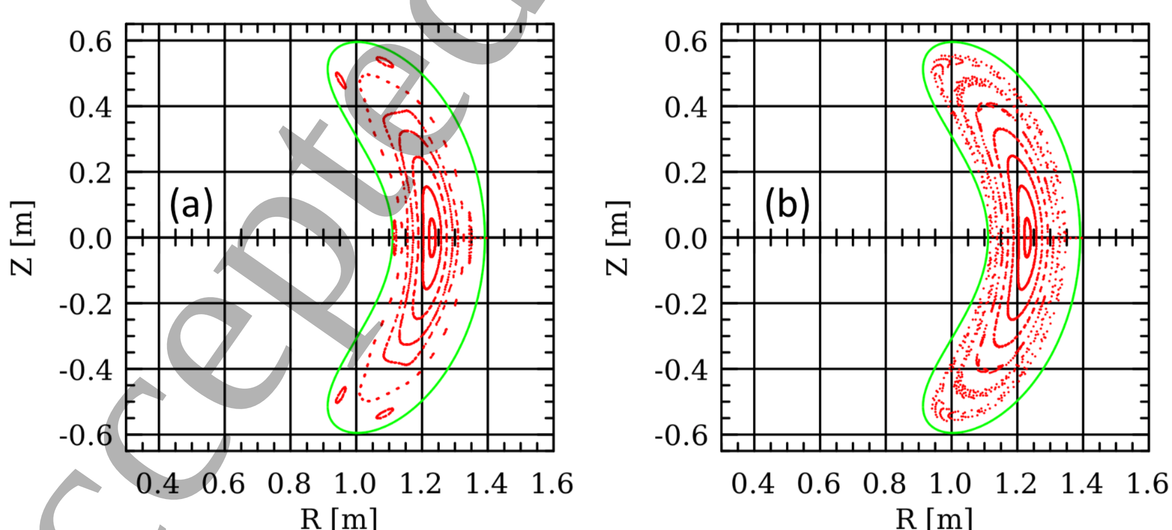

Figure 1. Poloidal cross sections with Poincaré plots of the magnetic configurations of two cases (a) with magnetic islands and (b) without magnetic island. Both figures are plotted at ϕ=0.

The following four parameters for the simulation are based on the CFQS design[4, 5]:

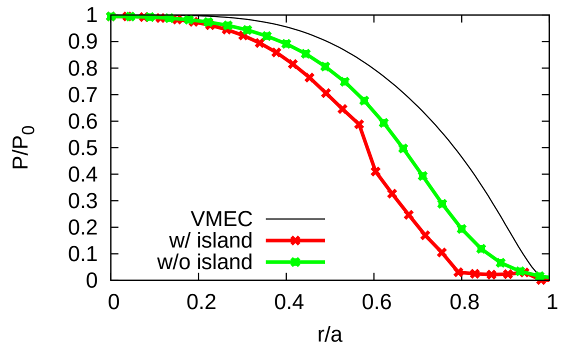

Figure 2. The normalized pressure profiles of VMEC, HINT with magnetic islands, and HINT without magnetic island. P_0 represents the pressure on the magnetic axis.

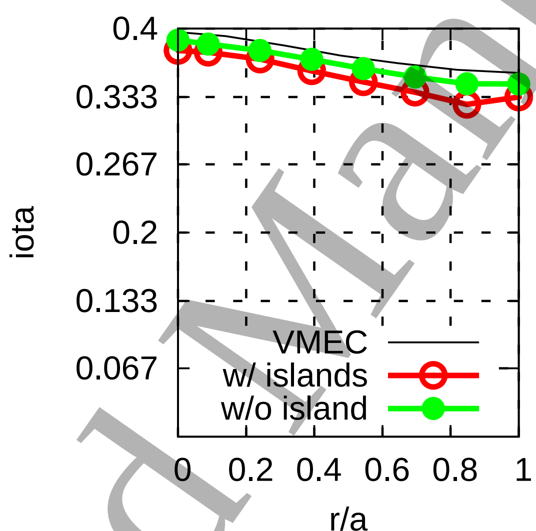

Figure 3. Rotational transform ι profiles of VMEC, HINT with magnetic islands, and HINT without magnetic island.

1) The plasma major radius $R_0 = 1.0$ m on average. 2) The magnetic field strength on the magnetic axis $B_0 = 1.0$ T on average. 3) The electron density in plasma center $n_e = 1.0 \times 10^{19}$ m^{-3}. 4) The electron temperature in plasma center $T_e = 2.1$ keV. And finally, 5) the β value of plasma in the core region is 1.0%. Hydrogen plasma is assumed, which is the same as the CFQS design. The number of field period N_{fp}=2, is the same as the CFQS design and equilibrium calculation. The neutral beam injection (NBI) system of the CFQS is transferred from the CHS device where the NBI energy $E_{NBI} = 40$ keV, and thus this parameter is used for the present work. A slowing-down energetic particle distribution function is assumed. In addition, a Gaussian-type pitch angle distribution function

$$f(\Lambda) = \exp[-\frac{(\Lambda - \Lambda_{peak})^2}{\Delta\Lambda^2}] \tag{8}$$

is assumed for the energetic particles, where $\Lambda = \mu B_0/E$ is the pitch angle variable,

μ is the magnetic moment, E is the particle energy, $\Lambda_{peak} = 0.1$ represents the pitch angle for the distribution peak, and $\Delta\Lambda = 0.2$ is a parameter to control the distribution width. Since NBI system of the CFQS has not been equipped yet, the above Λ_{peak} and $\Delta\Lambda$ parameters are set by reference to the Large Helical Device[19].

The number of computational particles is 32 million. Cylindrical coordinates (R, ϕ, z) are employed. Different from the previous simplified cases[19, 22, 23], in order to explore all possible toroidal mode numbers, the present work models the entire plasma with a toroidal range from $\phi = 0$ to $\phi = 2\pi$. The numbers of grid points in (R, ϕ, z) directions are (128, 256, 128), respectively.

3. Simulation results in the case with magnetic islands

3.1. Mode profiles in both three and two-dimensional form

The simulated mode profile of radial velocity v_{rad} is shown in Fig. 4. In the toroidal direction, only 3/4 tours are shown from $\phi = 0$ to $\phi = 1.5\pi$. The plasma from $\phi = 1.5\pi$ to $\phi = 2\pi$ is cut in order to better observe the poloidal cross section. The poloidal cross section on the left side is located at $\phi = 0$, while the one on the right side is located at $\phi = 1.5\pi$. They are bean-shaped and triangular, respectively. In the radial direction, only the plasmas whose pressure is greater than 0.83 maximum are displayed. In other words, the v_{rad} is plotted on the constant pressure surface where $P = 0.83P_{max}$, or the surface where $r/a = 0.4$. This surface is important because v_{rad} is strong there. It is clear that the poloidal mode number $m = 3$. On the bean-shaped cross section, v_{rad} is stronger than that on the triangular one. This is the first time to show instability in the CFQS in three-dimensional form.

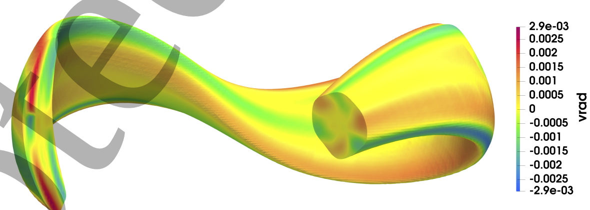

Figure 4. Radial velocity v_{rad} of the simulated mode in three-dimensional form. The orange and red represent the velocity from core to edge, while the green and blue represent the velocity from edge to core.

In order to better show the details of the velocity, its vortices at $\phi = 0$ and $\phi = 0.5\pi$ are shown in Fig. 5. Whether it is on the bean-shaped cross section or on the triangular one, it is easy to find three clockwise vortices and three counterclockwise ones. This suggests that the poloidal mode number $m = 3$. It can also be seen that on the bean-shaped cross section, in the direction from the center to the upper and lower ends, the velocity is larger than that of other places, including both the bean-shaped and triangular cross sections. This is the reason why in Fig. 4 the color of the bean-shaped cross section is stronger than that of the trangular one. The radial velocity v_{rad} is not toroidally symmetric.

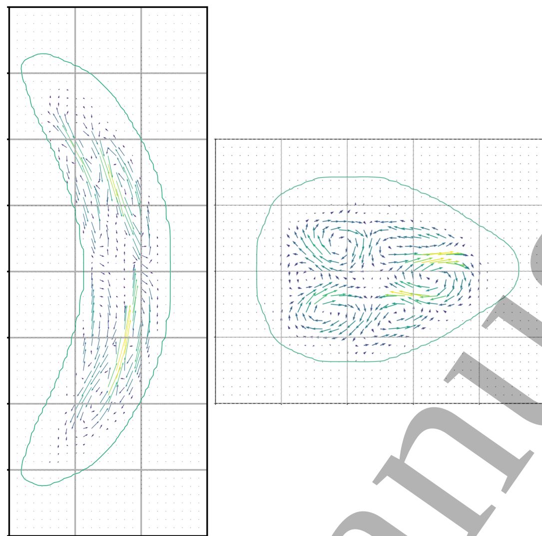

Figure 5. The velocity vortices at $\phi = 0$ (bean-shaped cross section) and $\phi = 0.5\pi$ (triangular cross section). The long red arrows represent a large velocity, while the short blue arrows represent a small velocity.

The mode profile in two-dimensional form is also analyzed, as shown in Fig. 6. All components with an absolute toroidal mode number less than 5 and a poloidal mode number less than 8 are analyzed. Only the strongest nine components are plotted; the remaining components are not plotted because they are weak. The dominant component is $m/n = 3/1$, as shown by the magenta line. The mode width is very large, and that means the simulated mode is a global one. The poloidal mode number agrees with those in Fig. 4 and Fig. 5. For the toroidal mode number, in addition to the n=1 component, the n=-1 and n=3 components cannot be neglected. This suggests very strong toroidal mode coupling, which is difficult to see in a tokamak, but can be seen on some stellarators like the LHD but not very strongly. This mode coupling phenomenon has been theoretically analyzed by Don Spong[24]. The toroidal components $n = n_0 + iN_{fp}$ are strong, where n_0 is the dominant toroidal mode number and it is 1 for Fig. 6, i is an arbitrary integer and it is -1, 0, and 1 for Fig. 6, N_{fp} is the number of the field period and it is 2 for the CFQS. Strong mode coupling happens under the condition of a very small N_{fp}. In the LHD stellarator, $N_{fp} = 10$ is relatively large, and thus the toroidal mode coupling is weak. The simulated mode coupling phenomenon in the present work is consistent with theoretical prediction[24] and also, it is similar to the simulation of the FAR3d code[8].

3.2. Mode frequency and growth rate

The dependence of mode frequency and growth rate on energetic particle beta β_{EP} (or energetic particle pressure) are analyzed, as shown in Fig. 7. The growth rate

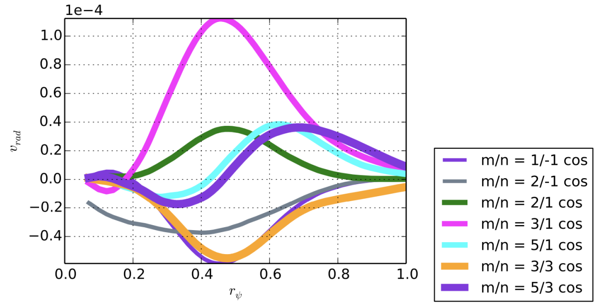

Figure 6. The mode profile of poloidal velocity v_{rad} in two-dimensional form.

increases with energetic particle pressure and this represents the simulated mode driven by energetic particles. This property is similar to that of Ref. [8]. But the mode frequency 79 kHz does not depend on energetic particles. It is close to the global Alfvén eigenmode (GAE) frequency[25] $(n - m\iota) \times \omega_A/(2\pi) = 78$ kHz, where $\omega_A = v_A/R_0 = 6.147 \times 10^6$ rad/s, where v_A is Alfvén velocity, $n = 1$, $m = 3$, $\iota = 1/q = 0.36$, and q is safety factor. This shows that the simulated mode is likely a GAE, or, an EPM located near the Alfvén continuum. In order to ensure the convergence of the simulation, different numbers of computational particles are loaded to compare with the usual results. In Fig. 7, closed triangles and closed circles are calculated with 32 million computational particles. At $\beta_{EP} = 0.4\%$, different numbers of computational particles are loaded, as shown by the open square and cross (8 million), and the open triangle and open circle (64 million). The points obtained under different computational particle numbers are consistent with each other, which confirms good convergence in the simulation.

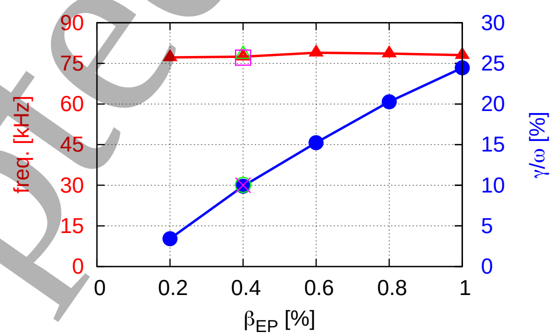

Figure 7. The dependence of mode frequency (triangles) and growth rate (circles) on energetic particle pressure. Closed triangles and closed circles are calculated with 32 million computational particles, the open square and cross are calculated with 8 million computational particles, and the open triangle and open circle are calculated with 64 million computational particles.

The time evolutions of different harmonics were also checked carefully. The frequencies of those harmonics were the same, but amplitudes were different. This shows that these harmonics constitute the same eigenmode.

Normally, NBI energy E_{NBI} is difficult to change, and thus, it is not necessary to scan the parameter E_{NBI}. But sometimes, in order to better understand the mode properties, it is still useful to investigate the mode behavior under different E_{NBI} parameters. The dependence of mode frequency and growth rate on E_{NBI} is analyzed, as shown in Fig. 8(a). The mode frequency does not depend on NBI energy. Growth rates in the cases of $E_{NBI} \leq 30keV$ are not plotted. The noises in these cases are too strong to accurately estimate the growth rate. But it is clear that the growth rates in these cases are apparently smaller than those in other cases. For the $E_{NBI} = 10$ keV case, the mode is stable.

The parallel velocities of resonant particles can be evaluated by analyzing energy transfer in Λ and E phase space. Roughly, $v_{\parallel} = \sqrt{1-\Lambda}\sqrt{2E/m_{EP}}$, where m_{EP} is the energetic particle mass. The ratio of $v_{\parallel}$ to v_A is shown in Fig. 8(b). The parallel velocities of resonant particles are close to $1/3v_A$, consistent with the AE destabilization condition[26]. This implies that the simulated mode may be an Alfvén eigenmode, or, an EPM located near the Alfvén continuum.

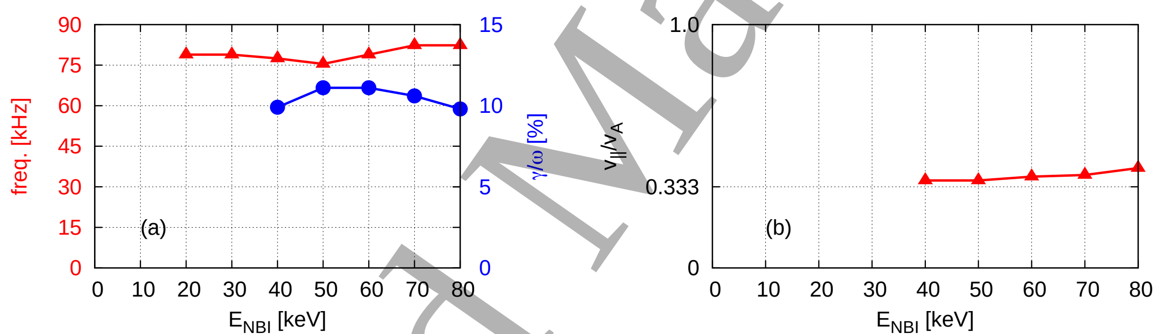

Figure 8. The dependence of (a) mode frequency (triangles) and growth rate (circles) and (b) the parallel velocity of resonant particles on NBI energy E_{NBI}.

The dependence of mode frequency and growth rate on the peak value of energetic particle pitch angle Λ_{peak} is also analyzed, but the conclusion is not clear. When changing Λ_{peak}, another mode appears and it has a strong influence on the present $m/n = 3/1$ mode. As a result, no clear trend is seen in the 3/1 mode, either in frequency or in growth rate. The phenomenon of multi-mode coexistence is very interesting, but it will not be discussed in this paper, but in another one.

3.3. Alfvén continuum

In order to identify the simulated mode, the Alfvén continuum is plotted in Fig. 9. This figure is analyzed using the STELLGAP code[24], which was developed for shear Alfvén continua in stellarators. In the present work, the STELLGAP code (version 7[27]) with sound wave coupling effects is conducted for analysis. The figure does not show data with a frequency that exceeds 200 kHz. Considering that the frequency of the simulated mode is only 79 kHz, the range of the vertical axis is reasonable. All components with an absolute toroidal mode number less than 4 and a poloidal mode number less than 10 are analyzed. But in the frequency range below 200 kHz, only three branches can be shown, and the other branches are outside this range. As calculated above, the frequency of the simulated mode is close to the GAE frequency. But near the mode location, there is not any extreme value of the $m/n = 3/1$ continuum. Considering the mode intersects with the continuum, it may be an EPM-like mode.

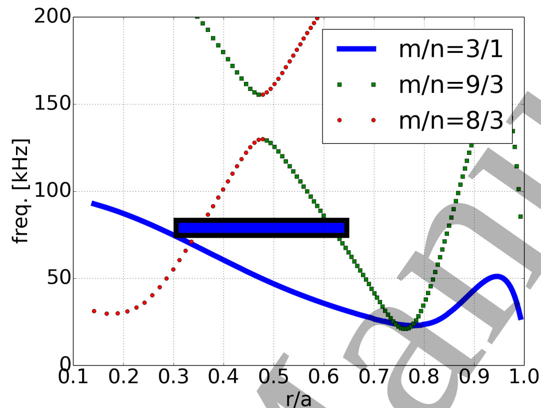

Figure 9. The Alfvén continuum in the case with magnetic islands.

3.4. Resonant condition

The simulated mode is driven by energetic particles through resonant interactions, and the frequency of mode, the frequency of toroidal motion f_ϕ, and the frequency of poloidal motion f_θ must satisfy the following resonant condition:

$$f_{mode} = nf_\phi - lf_\theta, \tag{9}$$

where f_{mode} is the mode frequency, n is the toroidal mode number, and l is an arbitrary integer[12, 28]. The resonant condition in Eq. (9) is general for toroidal plasmas, especially for tokamak plasmas. In the stellarator, there is a stronger theorem as follows[29]:

$$f_{mode} = Nf_\phi - Lf_\theta, \tag{10}$$

where $N = n + j\nu N_{fp}$, $L = m + j\mu$, $j = 0, \pm 1$, ν and μ are arbitrary integers. The resonances with non-zero j values are caused by the absence of axial symmetry and they are not often observed, even in stellarators. In order to analyze the resonant condition, 4096 particles with maximum δf values are marked and traced. The time for each particle to pass one round in the toroidal angle is defined as the toroidal period T_ϕ, and accordingly, a frequency $f_\phi = 1/T_\phi$. Similarly, in the poloidal direction, T_θ and f_θ are defined. In order to reduce the error, after the 4096 particles were marked, they were continuously traced for about 0.9 ms (about 70 mode periods) to calculate the average value of f_ϕ and f_θ. As a result, the relationship of particle frequencies f_ϕ and

f_θ is plotted in Fig. 10(a). The solid green line representing $f_\phi = 2.33 f_\theta + 26.33$ kHz or $f_{mode} = 3f_\phi - 7f_\theta$ passes through most of the red dots. The dotted blue line representing $f_\phi = 2f_\theta + 79$ kHz or $f_{mode} = f_\phi - 2f_\theta$ also passes through many red dots. Since the solid green line fits the red dots better than the dotted blue line, it confirms that $n = 1$, $j = 1$, $\nu = 1$, $m = 3$, $\mu = 4$, and $L = 7$ in Eq. (10) are dominant for the simulated mode. The resonance of $j = 1$ becomes dominant, which is caused by the absence of axial symmetry. More specifically, in the CFQS, this is caused by the 2-fold rotational symmetry of the equilibrium magnetic field. In addition, although the distribution ranges of f_ϕ and f_θ are wide, the distribution width in the direction perpendicular to the green line is still narrow, which shows that the data is reliable. The dashed pink line representing $f_\phi = f_\theta + 79$ kHz or $f_{mode} = f_\phi - f_\theta$ passes through a few red dots located at a low energy region where $f_\theta \approx 45$ kHz and $f_\phi \approx 125$ kHz. This suggests that $n = 1$, $j = 0$, and $L = 1$ in Eq. (9) are subdominant for the simulated mode. Particles satisfying various resonant conditions appear simultaneously. The L value in Eq. (10) is directly shown in Fig. 10(b) for $n = 1$, $j = 1$, and $L = 7$. They are also shown in Fig. 10(c) for $n = 1$, $j = 0$ and $L = 1$. In Fig. 10(b), most particles are located around $L = 7$, while in Fig. 10(c), many particles are located around $L = 2$ but the bias is relatively large, especially in the low f_θ region. This confirms again that $n = 1$, $j = 1$, and $L = 7$ in Eq. (10) are dominant for the simulated mode. In Fig. 10(c), a few particles are perfectly located at $L = 1$. This confirms again that in Eq. (9) $n = 1$, $j = 0$, and $L = 1$ are subdominant.

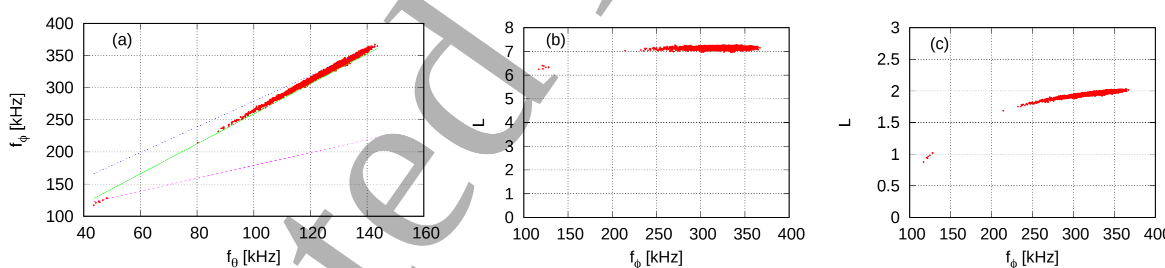

Figure 10. (a) The relationship of particle frequencies f_ϕ and f_θ of 4096 particles with maximum δf values. The solid green line represents $f_{mode} = 3f_\phi - 7f_\theta$, the dotted blue line represents $f_{mode} = f_\phi - 2f_\theta$, and the dashed pink line represents $f_{mode} = f_\phi - f_\theta$. (b) The L values of 4096 resonant particles for $n = 1$ and $j = 1$. (c) The L values of 4096 resonant particles for $n = 1$ and $j = 0$.

3.5. Nonlinear frequency chirping and hole-clump formation in phase space

All of the above analysis is carried out in the linear growth phase. In this subsection, the mode time evolution and frequency spectrum in both linear growth phase and nonlinear saturated phase are investigated, as shown in Fig. 11. The mode frequency in the linear growth phase is 79 kHz. At $t = 0.32$ ms, the mode amplitude becomes maximum, and then the mode steps into a nonlinear saturated phase and the mode frequency starts to chirp down. After about 0.1 ms, the mode frequency has already chirped down to 70 kHz. This is the first time to show frequency chirping in the CFQS.

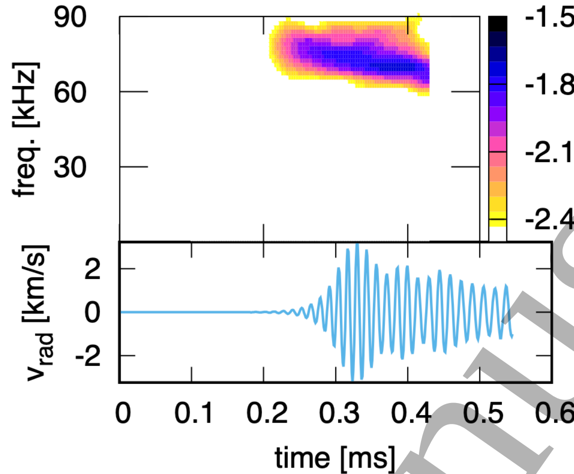

Figure 11. The time evolution of (top) frequency spectrum and (bottom) radial velocity v_{rad}. Both panels share the horizontal axis. The color bar indicates the magnitude in logarithmic scale.

The energetic particle energy transfer $\delta f \times dE/dt$ of all simulation particles is analyzed in the phase space of pitch angle Λ and energy E, as shown in Fig. 12. The $\delta f \times dE/dt$ is mainly marked in purple, which represents $\delta f \times dE/dt < 0$, energy transfers from energetic particles to the mode, and it is destabilized. The five curves represent constant resonance frequencies f_{res}, which are evaluated by $f_{res} = kf_{\theta Approx}$. The constant k is a coefficient. $f_{\theta Approx} = \sqrt{1-\Lambda}\sqrt{2E/m_{EP}}/(2\pi q R_0)$ is the approximate poloidal frequency calculated from the values of Λ and E. In ideal case with zero orbit width, $f_\phi = qf_\theta$, then, $f_{res} = kf_\theta$ where $k = Nq - L$. In the realistic case, f_ϕ is not simply qf_θ, and f_{res} can not be simply shown in (Λ, E) space, but f_{res} can be roughly evaluated in a statistical way. In Fig. 10, 4096 particles were investigated and their resonance frequencies, energies, and pitch angles are known. The coefficient $k = 0.586$ can be obtained by plotting 4096 particles and curve fitting in a figure of f_{res} versus $f_{\theta Approx}$. From bottom to top, these five curves represent $f_{res} = 50$ kHz, 60 kHz, 70 kHz, 80 kHz, and 90 kHz, respectively. Although constant f_{res} curves calculated in this figure are not as exact as those in Fig. 10, they are still good references for observing frequency changes. In the left subfigure, the purple part is located around $f_{res} = 75$ kHz. While in the right subfigure, the location of the purple part changes, and it is located around $f_{res} = 65$ kHz. The purple part moves from the high frequency region to the low frequency one during mode frequency chirping down.

The energetic particle distribution δf of all simulation particles is also analyzed in (Λ, E) space, as shown in Fig. 13. The blue color represents $\delta f < 0$ (hole) while the red color represents $\delta f > 0$ (clump). The δf distribution is integrated over the whole simulation domain. In the left subfigure, the hole is located on the blue curve representing $f_{res} = 80$ kHz, and the center of the hole region is slightly above the

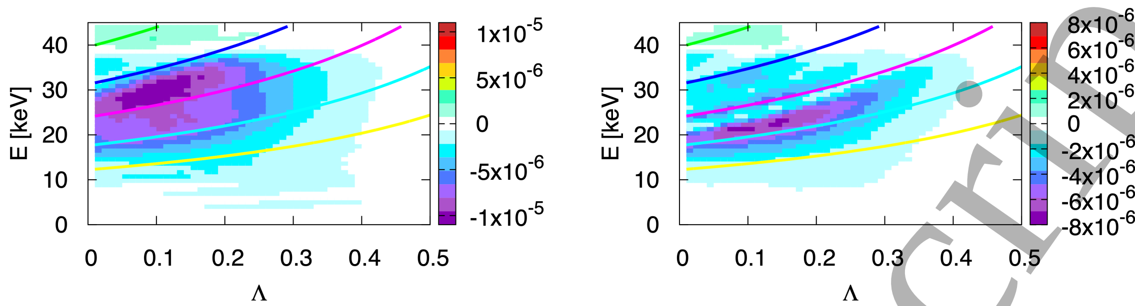

Figure 12. The energetic particle energy transfer $\delta f \times dE/dt$ in (Λ, E) space at (left) $t = 0.34$ ms and (right) $t = 0.50$ ms. The five curves represent constant f_{res} curves from 50 kHz to 90 kHz.

blue curve. While in the right subfigure, the center of the hole region moves slightly rightward, and just below the blue curve. The hole structure moves slightly from the high frequency region to the low frequency one during mode frequency chirping down. The clump frequency also slightly decreases. In the left subfigure, the center of the clump region is located slightly above the $f_{res} = 60$ kHz curve, while in the right subfigure, it is located between $f_{res} = 50$ kHz and $f_{res} = 60$ kHz. The movement of hole and clump indicates that the particles comprising the hole and clump are kept resonant with the mode during the frequency chirping. In Fig. 13, there is another hole-clump pair in the low energy region where $E < 10$ keV. By mapping the 4096 particles of Fig. 10 into (Λ, E) space, it is easy to identify that in Fig. 13 the particles in the large hole-clump pair (or in the high energy region) satisfy the resonant condition with $j = 1$, while the particles in the small hole-clump pair (or in the low energy region) satisfy the resonant condition with $j = 0$. Again, particles satisfying various resonant conditions appear simultaneously.

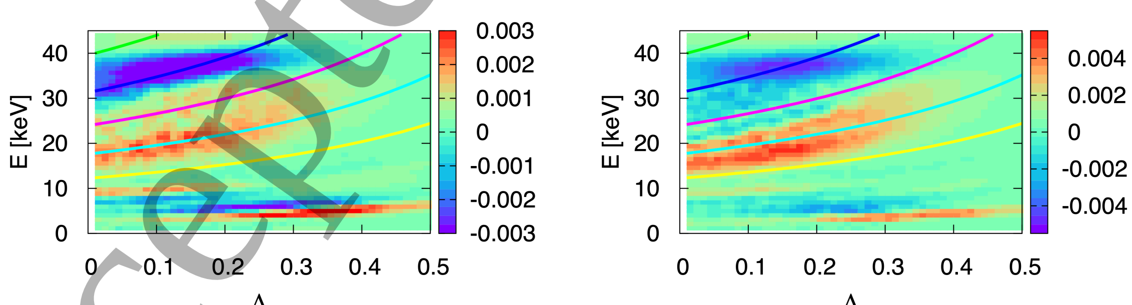

Figure 13. The energetic particle distribution δf in (Λ, E) space at (left) $t = 0.34$ ms and (right) $t = 0.50$ ms. The five curves represent constant f_{res} curves from 50 kHz to 90 kHz.

3.6. Energetic particle radial transport

Energetic particle radial transport can be seen from the change of the energetic particle pressure profile, and thus, the energetic particle pressure profiles at different times are plotted in Fig. 14. Compared with that in the initial phase, the energetic particle pressure in the core region is reduced by about 15% at the moment of maximum mode amplitude. This indicates strong energetic particle radial transport.

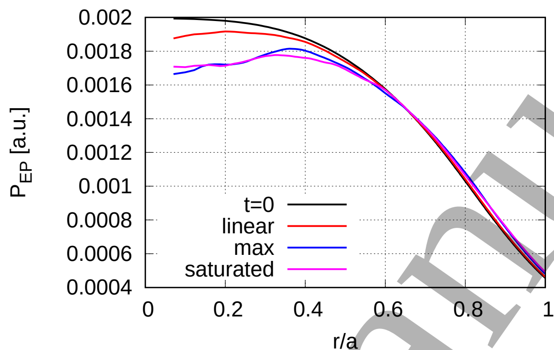

Figure 14. The energetic particle pressure profiles of the mode in the initial and linear growth phases, at the moment of maximum amplitude, and in the nonlinear saturated phase.

4. Simulation results in the case without magnetic island

4.1. Mode profiles

The mode profile is analyzed and shown in Fig. 15. Similar to that in Fig. 6, only the strongest twelve components are plotted. The dominant component is $m/n = 5/2$. For the toroidal mode number, in addition to the $n = 2$ component, the $n = -2$, $n = 0$, and $n = 4$ components cannot be neglected. Similar to that in Fig. 6, this suggests very strong toroidal mode coupling which is difficult to see in a tokamak.

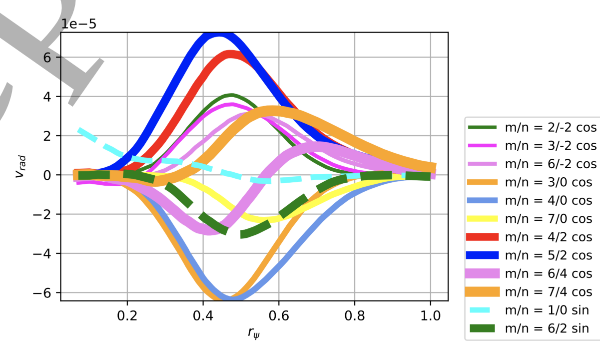

Figure 15. The mode profile of poloidal velocity v_{rad} in the case without magnetic island.

4.2. Mode frequency and growth rate

The dependence of mode frequency and growth rate on energetic particle beta β_{EP} (or energetic particle pressure) are analyzed, as shown in Fig. 16. Similar to that in Fig. 7, the growth rate increases with energetic particle pressure which represents that the simulated mode is driven by energetic particles. But the mode frequency 125 kHz does not depend on energetic particles.

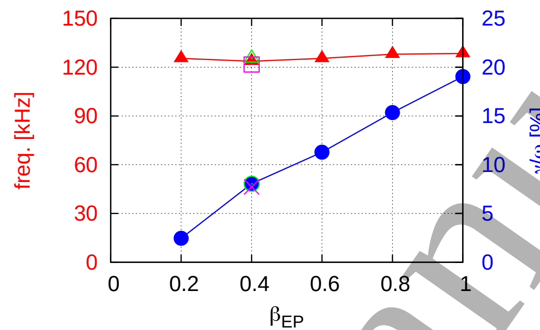

Figure 16. The dependence of mode frequency (triangles) and growth rate (circles) on energetic particle pressure. Closed triangles and closed circles are calculated with 32 million computational particles, the open square and cross are calculated with 8 million computational particles, and the open triangle and open circle are calculated with 64 million computational particles.

Similar to that in Sec. 3, the frequencies of different harmonics are the same, but amplitudes are different. This shows that these harmonics constitute the same eigenmode.

The dependence of mode frequency and growth rate on E_{NBI} is also analyzed. For the cases where $E_{NBI} \leq 20$ keV and those where $E_{NBI} \geq 70$ keV, the mode is stable. For the cases where 30 keV $\leq \mathrm{E_{NBI}} \leq$ 60 keV, the mode frequency does not depend on NBI energy.

The dependence of mode frequency and growth rate on the peak value of energetic particle pitch angle Λ_{peak} is also analyzed, as shown in Fig. 17. The mode frequency 125 kHz does not depend on Λ_{peak}. The growth rate decreases with the increasing of Λ_{peak}, except those points at $\Lambda_{peak} = 0.5$ and $\Lambda_{peak} = 0.6$. At those points, the mode keeps stable. The stabilization may be cause by the transition from the passing particles to the trapped particles. According to this figure, in order to suppress the simulated mode, it is better not to inject the neutral beam tangentially.

4.3. Alfvén continuum

From the above analysis, it can be seen that the simulated mode is very likely to be an Alfvén eigenmode. At $\iota \approx 0.3636$ or $\iota \approx \frac{2}{(5+6)/2}$, indeed, a TAE with $m/n = 5/2$ and $m/n = 6/2$ is possible to be excited. For better analysis, the Alfvén continuum is plotted using the STELLGAP code in Fig. 18. The harmonics $m/n = 5/2$ and

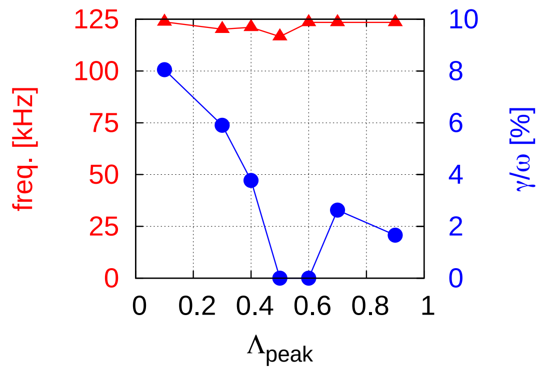

Figure 17. The dependence of mode frequency (circle) and growth rate (triangle) on the peak value of energetic particle pitch angle Λ_{peak}.

$m/n = 6/2$ constitute a gap, and the simulated 5/2 mode is just below the gap. The STELLGAP code is conducted based on the VMEC equilibrium, but the MEGA code is conducted based on the HINT equilibrium. Considering the differences between VMEC and HINT (or the differences between STELLGAP and MEGA), the mode may be located inside but not below the gap. Thus, the simulated mode may be the toroidal Alfvén eigenmode (TAE).

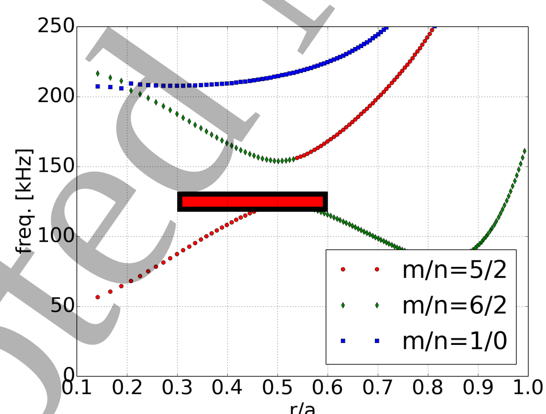

Figure 18. The Alfvén continuum in the case without magnetic island.

4.4. Resonant condition

In order to analyze the resonant condition, similar to that in Sec. 3, 4096 particles with maximum δf values were analyzed. The relationship of particle frequencies f_ϕ and f_θ is plotted in Fig. 19(a). The solid green line representing $f_{mode} = 4f_\phi - 9f_\theta$ perfectly passes through most of these red dots. The dotted blue line representing $f_{mode} = 2f_\phi - 4f_\theta$ also passes through many red dots. Again, the resonance of $j = 1$ becomes dominant, which is caused by the 2-fold rotational symmetry of the equilibrium magnetic field. The dashed pink line representing $f_{mode} = 2f_\phi - 3f_\theta$ passes through a few red dots located at the low energy region where $f_\theta \approx 55$ kHz and $f_\phi \approx 145$ kHz. Particles satifsfying various j values of the resonant condition appear simultaneously. The L values in Eq. (10) are directly shown in Fig. 19(b) for $n = 2$, $j = 1$ and $L = 9$. They are also shown in Fig. 19(c) for $n = 2$, $j = 0$ and $L = 4$.

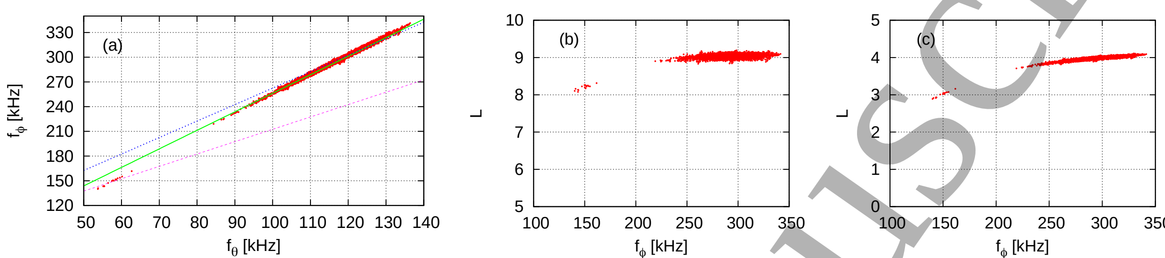

Figure 19. (a) The relationship of particle frequencies f_ϕ and f_θ of 4096 particles with maximum δf values. The solid green line represents $f_{TAE} = 4f_\phi - 9f_\theta$, the dotted blue line represents $f_{TAE} = 2f_\phi - 4f_\theta$, and the dashed pink line represents $f_{TAE} = 2f_\phi - 3f_\theta$. (b) The L values of 4096 resonant particles for $n = 2$ and $j = 1$. (c) The L values of 4096 resonant particles for $n = 2$ and $j = 0$.

4.5. Nonlinear frequency chirping and hole-clump formation in phase space

In this subsection, the mode time evolution and frequency spectrum in both linear growth and nonlinear saturated phases are investigated, as shown in Fig. 20. The dominant branch chirps down to 105 kHz, while another branch chirps up to 140 kHz but it is weak.

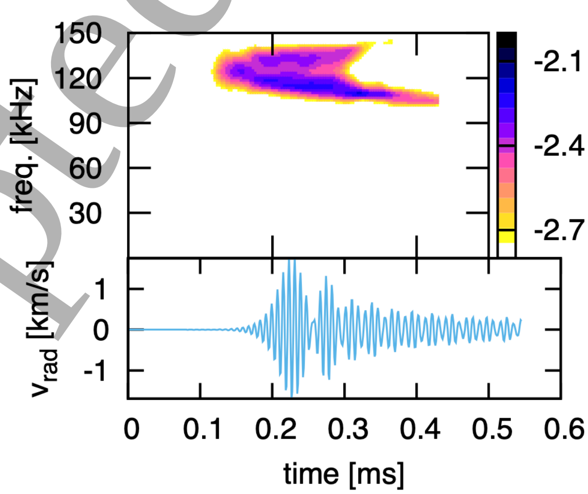

Figure 20. The time evolution of (top) frequency spectrum and (bottom) radial velocity v_{rad}. Both panels share the horizontal axis. The color bar indicates the magnitude in logarithmic scale.

The energetic particle energy transfer $\delta f \times dE/dt$ of all simulation particles is analyzed in the phase space of pitch angle Λ and energy E, as shown in Fig. 21.

Similar to that in the EPM-like mode case, the seven curves represent $f_{res} = kf_{\theta Approx}$ where $k = 1.126$. At $t = 0.19$ ms, the $\delta f \times dE/dt$ is mainly negative, and the TAE is destabilized. Those particles that provide energy for the TAE are mainly located around $f_{res} = 130$ kHz. At $t = 0.36$ ms, the $\delta f \times dE/dt$ is still mainly negative, but the purple part is split into two independent parts. These two parts are located around $f_{res} = 150$ kHz and $f_{res} = 110$ kHz, and they correspond to the high and low frequency branches of the TAE in Fig. 20. The two purple parts move during the frequency chirping of the two branches of the TAE.

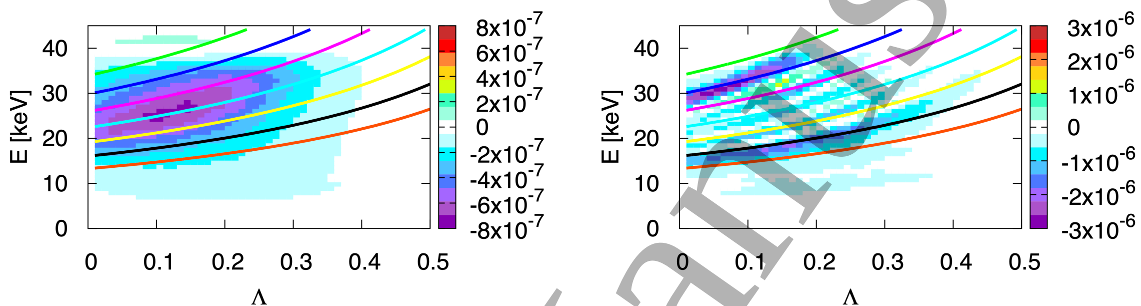

Figure 21. The energetic particle energy transfer $\delta f \times dE/dt$ in (Λ, E) space at (left) $t = 0.19$ ms and (right) $t = 0.36$ ms. The seven curves represent constant f_θ curves or constant f_{res} curves from 100 kHz to 160 kHz.

The energetic particle distribution δf of all simulation particles is also analyzed in (Λ, E) space, as shown in Fig. 22. At $t = 0.19$ ms, the hole is located around $f_{res} = 135$ kHz. While at $t = 0.36$ ms, the hole moves upward to $f_{res} = 150$ kHz. Also, at $t = 0.19$ ms, the clump is located around $f_{res} = 125$ kHz, while at $t = 0.36$ ms, the clump moves downward to $f_{res} = 105$ kHz. The movement of hole and clump indicates that the particles comprising them are kept resonant with the TAE during the frequency chirping. In Fig. 22, there is another hole-clump pair in the low energy region where $E \approx 10$ keV. In Fig. 22 the particles in the large hole-clump pair (or in the high energy region) satisfy the resonant condition with $j = 1$, while the particles in the small hole-clump pair (or in the low energy region) satisfy the resonant condition with $j = 0$.

4.6. Energetic particle radial transport

Similar to that in Fig. 14, the energetic particle pressure profiles at different times are plotted in Fig. 23, to see the energetic particle radial transport. Compared with that in the initial phase, the energetic particle pressure in the core region is reduced by about 7% at the moment of maximum TAE mode amplitude. Comparing Fig. 14 and Fig. 23, it can be seen that the transport caused by the EPM-like mode in the present simulation is stronger. The difference between Fig. 14 and Fig. 23 can be explained by the following reasons. First, in the present simulations, both the TAE growth rate and TAE maximum amplitude are weaker than that of the EPM-like mode. Second,

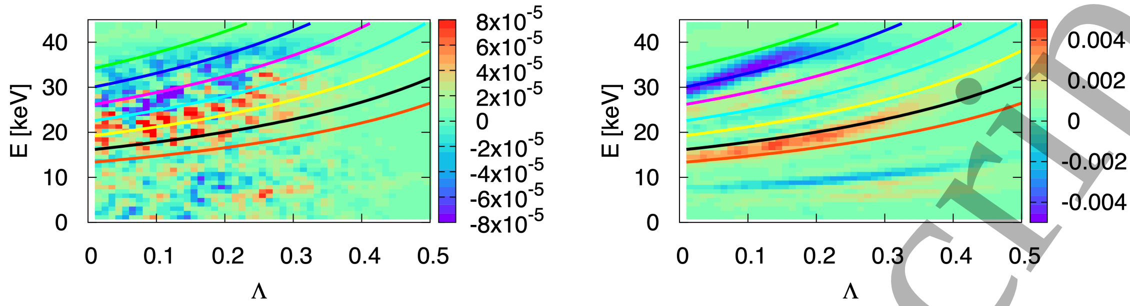

Figure 22. The energetic particle distribution δf in (Λ, E) space at (left) $t = 0.19$ ms and (right) $t = 0.36$ ms. The seven curves represent constant f_θ curves or constant f_{res} curves from 100 kHz to 160 kHz.

energetic particles are initially loaded at $t = 0$, and after that, energetic particles are continuously transported with time. In Fig. 14, the mode amplitude becomes maximum at $t = 0.32$ ms, while in Fig. 23 the mode amplitude becomes maximum at $t = 0.19$ ms. The analysis of the EPM-like mode in Fig. 14 is significantly later than that of the TAE in Fig. 23, and more particles are transported.

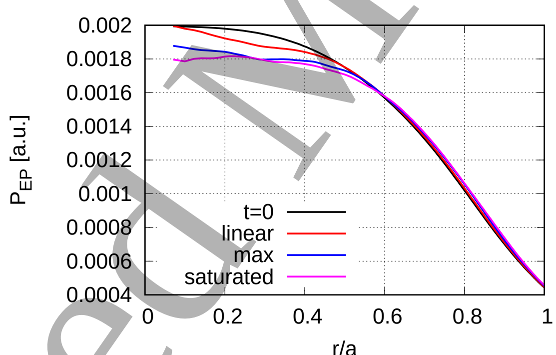

Figure 23. The energetic particle pressure profiles of the TAE in the initial and linear growth phases, at the moment of maximum amplitude, and in the nonlinear saturated phase.

5. Summary

In summary, the nonlinear simulations of energetic particle driven instabilities in the CFQS are conducted using the MEGA code for the first time. The simulation parameters are based on the CFQS design. Two equilibria with and without magnetic islands are considered. The instability in the CFQS in three-dimensional form is shown for the first time. Both the EPM-like mode and TAE are found in the CFQS with and without magnetic islands. The dominant mode numbers are $m/n = 3/1$ for the EPM-like mode and $m/n = 5/2$ for the TAE. Strong mode coupling is found under the condition of a very low number of field period N_{fp} value. This result is consistent with theoretical prediction[24], and it is similar to the simulation of the FAR3d code[8]. For the EPM-like mode, the mode frequency 79 kHz does not depend on energetic particle pressure or energetic particle beam velocity, while the growth rate increases with energetic particle pressure, and the growth rate is maximum for the energetic particle beam velocity of $0.5v_A$. For the TAE, similarly, the mode frequency 125 kHz does not depend on energetic particle pressure, energetic particle beam velocity, or the peak value of energetic particle pitch angle. The growth rate increases with energetic particle pressure, roughly decreases with the increasing of the peak value of energetic particle pitch angle, and the growth rate is maximum for the energetic particle beam velocity of $0.5v_A$. For the EPM-like mode, the resonant condition $f_{mode} = 3f_\phi - 7f_\theta$ is dominant and $f_{mode} = f_\phi - f_\theta$ is subdominant. For the TAE, the resonant condition $f_{mode} = 4f_\phi - 9f_\theta$ is dominant and $f_{mode} = 2f_\phi - 3f_\theta$ is subdominant. The 2-fold rotational symmetry of the equilibrium magnetic field plays important roles in the resonances of both modes. This kind of resonance is not often observed, even in stellarators. Also, the mode frequencies chirp in the nonlinear saturated phase. Hole and clump structures are formed in the pitch angle and energy phase space. The particles comprising the hole and clump are kept resonant with the modes during the mode frequencies chirping. Finally, during the mode activities, energetic particles are transported from the core region. For the present simulation, the transport caused by the EPM-like mode is stronger than that of the TAE.

For the CFQS operation, it should be noted that even if the ι profile is only slightly changed, the properties of the instability may be greatly affected. For example, the excited mode changes from the EPM-like mode to the TAE. This conclusion is similar to that of Ref. [8]. In addition, in order to reduce or even completely suppress the EPM-like mode or TAE, it is worth trying to adjust the energetic particle beam velocity or the beam injection angle. Another possible way is to change the v_A by adjusting the magnetic field strength or plasma density, so that the energetic particle velocity avoids values around $0.5v_A$.

The present research leaves some interesting gaps. During the change of Λ_{peak}, in the case with magnetic islands, the phenomenon of multi-mode coexistence occurs. How these modes interact is an interesting subject. In the case without a magnetic island, the TAE is stable around $\Lambda_{peak} \approx 0.5$, and the reason is still unclear. In addition, the Alfvén-sound coupling was found in W7-AS[30], but it has not been discussed in CFQS. The above gaps may be filled in future work.

Acknowledgments

Numerical computations were performed on the "Plasma Simulator" (NEC SX-Aurora TSUBASA) of National Institute for Fusion Science (NIFS) with the support and under the auspices of the NIFS Collaboration Research program (NIFS19KNXN397, NIFS20KNST156, NIFS21KNST196, and NIFS22KIST025), the JFRS-1 supercomputer system at Computational Simulation Centre of International Fusion Energy Research

Centre (IFERC-CSC), and the Supercomputer Fugaku provided by the RIKEN Center for Computational Science (Project IDs: hp200127, hp210178). This work was partly supported by MEXT as "Program for Promoting Researches on the Supercomputer Fugaku (Exploration of burning plasma confinement physics, JPMXP1020200103)", JSPS KAKENHI Grant No. JP18K13529, No. JP18H01202, and "PLADyS", JSPS Core-to-Core Program, A. Advanced Research Networks. The authors thank Dr. D. Spong of ORNL for kindly providing the STELLGAP code. Also, the authors thank Prof. Y. Xu of SWJTU, Prof. M. Isobe of NIFS, Prof. S. Okamura of NIFS, Prof. K. Nagasaki of Kyoto Univ., Dr. J. Huang of SWJTU, Dr. J. Wang of NIFS, Dr. M. Idouakass of NIFS, Prof. G. Fu of ZJU, and Mr. H. Li of Univ. Tokyo for their sincere help and fruitful discussions.

References

[1] Xu Y 2016 *Matter and Radiation at Extremes* **1** 192–200

[2] OKAMURA S, MATSUOKA K, NISHIMURA S, ISOBE M, SUZUKI C, SHIMIZU A, NOMURA I, IDA K, FUJISAWA A, MURAKAMI S, NAKAJIMA N and YOKOYAMA M 2002 *Journal of Plasma and Fusion Research* **78** 166–179

[3] Nelson B, Berry L, Brooks A, Cole M, Chrzanowski J, Fan H M, Fogarty P, Goranson P, Heitzenroeder P, Hirshman S, Jones G, Lyon J, Neilson G, Reiersen W, Strickler D and Williamson D 2003 *Fusion Engineering and Design* **66-68** 169–174 ISSN 0920-3796 22nd Symposium on Fusion Technology

[4] SHIMIZU A, LIU H, ISOBE M, OKAMURA S, NISHIMURA S, SUZUKI C, XU Y, ZHANG X, LIU B, HUANG J, WANG X, LIU H, TANG C and the CFQS Team 2018 *Plasma and Fusion Research* **13** 3403123

[5] ISOBE M, SHIMIZU A, LIU H, LIU H, XIONG G, YIN D, OGAWA K, YOSHIMURA Y, NAKATA M, KINOSHITA S, OKAMURA S, TANG C, XU Y and the CFQS Team 2019 *Plasma and Fusion Research* **14** 3402074

[6] Liu H, Shimizu A, Xu Y, Okamura S, Kinoshita S, Isobe M, Li Y, Xiong G, Wang X, Huang J, Cheng J, Liu H, Zhang X, Yin D, Wang Y, Murase T, Nakagawa S and Tang C 2020 *Nuclear Fusion* **61** 016014

[7] Wang X, Xu Y, Shimizu A, Isobe M, Okamura S, Todo Y, Wang H, Liu H, Huang J, Zhang X, Liu H, Cheng J and Tang C 2021 *Nuclear Fusion* **61** 036021

[8] Varela J, Shimizu A, Spong D, Garcia L and Ghai Y 2021 *Nuclear Fusion* **61** 026023

[9] Heidbrink W and Sadler G 1994 *Nuclear Fusion* **34** 535–615

[10] Chen L 1994 *Physics of Plasmas* **1** 1519

[11] Briguglio S Z F and G V 1998 *Physics of Plasmas* **5** 3287

[12] Heidbrink W W 2008 *Physics of Plasmas* **15** 055501

[13] Todo Y 2006 *Physics of Plasmas* **13** 082503

[14] Todo Y, Berk H and Breizman B 2010 *Nuclear Fusion* **50** 084016

[15] Todo Y, Seki R, Spong D A, Wang H, Suzuki Y, Yamamoto S, Nakajima N and Osakabe M 2017 *Physics of Plasmas* **24** 081203 ISSN 1089-7674

[16] Park W, Parker S, Biglari H, Chance M, Chen L, Cheng C Z and Hahm T S 1992 *Physics Fluids B* **4** 2033

[17] Bierwage A Todo Y A N and K S 2016 *Nuclear Fusion* **56** 106009

[18] Sato M and Todo Y 2020 *Journal of Plasma Physics* **86** 815860305

[19] Wang H, Todo Y, Oasakabe M, Ido T and Suzuki Y 2019 *Nuclear Fusion* **59** 096041

[20] Hirshman S P and Whitson J C 1983 *The Physics of Fluids* **26** 3553–3568

[21] Suzuki Y, Nakajima N, Watanabe K, Nakamura Y and Hayashi T 2006 *Nuclear Fusion* **46** L19

[22] Wang H, Todo Y, Ido T and Suzuki Y 2018 *Phys. Rev. Lett.* **120**(17) 175001

[23] Wang H, Todo Y, Osakabe M, Ido T and Suzuki Y 2020 *Nuclear Fusion* **60** 112007

[24] Spong D A, Sanchez R and Weller A 2003 *Physics of Plasmas* **10** 3217–3224

[25] Li Y M and Ross D 1987 *Physics of Fluids* **30** 1466

[26] Kerner W, Borba D, Huysmans G T A, Porcelli F, Poedts S, Goedbloed J P and Betti R 1994 *Plasma Physics and Controlled Fusion* **36** 911

[27] Spong D A 2021 Stellgap `https://github.com/ORNL-Fusion/Stellgap`

[28] Todo Y 2019 *Reviews of Modern Plasma Physics* **3** 1

[29] Kolesnichenko Y I, Lutsenko V V, Wobig H and Yakovenko V 2002 *Physics of Plasmas* **9** 517

[30] Kolesnichenko Y I, Lutsenko V V, Weller A, Werner A, Yakovenko Y V, Geiger J and Fesenyuk O P 2007 *Physics of Plasmas* **14** 102504